Article:
Kaur, Channprit, Chaurasia, S., Singh, Narendra et al. (3 more authors) (2019) L-shell spectroscopy of neon and fluorine like copper ions from laser produced plasma. Physics of Plasmas. 023301. ISSN: 1089-7674

https://doi.org/10.1063/1.5051758

L-shell spectroscopy of neon and fluorine like copper ions from laser produced plasma

Cite as: Phys. Plasmas **26**, 023301 (2019); https://doi.org/10.1063/1.5051758
Submitted: 12 August 2018 . Accepted: 11 January 2019 . Published Online: 07 February 2019

Channprit Kaur, S. Chaurasia, Narendra Singh, John Pasley, Sunny Aggarwal, and Man Mohan

Physics of Plasmas ARTICLE scitation.org/journal/php

L-shell spectroscopy of neon and fluorine like copper ions from laser produced plasma

Cite as: Phys. Plasmas **26**, 023301 (2019); doi: 10.1063/1.5051758
Submitted: 12 August 2018 · Accepted: 11 January 2019 ·
Published Online: 7 February 2019

Channprit Kaur,[1,2] S. Chaurasia,[1,2,a)] Narendra Singh,[3] John Pasley,[4] Sunny Aggarwal,[3] and Man Mohan[3]

AFFILIATIONS

[1]High Pressure and Synchrotron Radiation Physics Division, BARC, Mumbai 400085, India
[2]Homi Bhabha National Institute, Mumbai 400094, India
[3]Delhi University, Delhi 110007, India
[4]York Plasma Institute, Department of Physics, University of York, York, YO10 5DQ, United Kingdom

[a)]**Email:** shibu@barc.gov.in

ABSTRACT

Ne, F, and O-like Rydberg resonance lines along with some of the inner shell satellite lines of Copper plasma, in the wavelength range of 7.9–9.5 Å, are experimentally observed using a thallium acid phthalate crystal spectrometer. The plasma is produced by the irradiation of a Cu target with a 15 J, 500 ps Nd: Glass laser with a focusable intensity up to 5×10^{14} W/cm^2. The observed lines result from the transitions among 2p-nd, 2p-ns, and 2s-nd (n = 4–6) levels. Transition wavelengths, transition probabilities, and oscillator strengths of these lines are calculated using the Multi-Configuration Dirac-Fock method. In this computation, the contribution of relativistic corrections such as two-body Breit corrections and QED corrections due to vacuum polarization and self-energy has also been considered. FLYCHK simulations are used to analyze the distribution of the various charge states of the Copper ions and to find the temperature and density of plasma. Moreover, the effect of self-absorption of the plasma (opacity), as well as of suprathermal electrons on charge state distribution of ions, is also studied. The synthetic spectrum provides a best-match with the experimental spectrum at a laser intensity of 1.3×10^{14} W/cm^2 for $T_c = 150$ eV, $T_h = 1000$ eV, $f = 0.008$, and density 4.5×10^{20} cm^{-3}.The temperature and density ranges are also calculated using a radiative hydrodynamic code. The calculated temperature and density range are in agreement with the experimentally determined values. The effect of the change in laser intensity on the L-shell spectrum of Cu is studied which indicates the switching between lower (Cu XX) and higher charge states (Cu XXI and Cu XXII) at higher laser intensities.

I. INTRODUCTION

The hot dense plasma, produced by high power lasers, has attracted attention in various fields such as high energy density physics and atomic physics and as a source of bright X-rays. The soft and hard X-rays produced from laser-produced plasma are useful for diagnosing conditions in dense plasma experiments.[1–5] X-rays are produced from plasma via free-free, free-bound, and bound-bound transitions occurring in highly charged ions present in the plasma.[6] The X-ray line emission from bound-bound transitions from highly charged ions has proven to be an excellent method to obtain a wealth of information about the plasma. K-shell emission can easily be achieved by interacting a moderately intense laser with a low Z target. Extensive studies of K-shell emission spectra from laser-produced plasma have been carried out in the past.[7–18] The relative ease with which K-shell spectra can be modelled makes them an obvious target for study. On the other hand, although the L-shell ionization of high Z atoms can be achieved easily, complex models are required to interpret such spectra. L-shell ions are observed in many astrophysical phenomena and in the laboratory. In astrophysics, the radiation produced by highly charged ions is a key observable from the standpoint of diagnosing the physical properties of non-terrestrial sources. L-shell spectroscopy provides a means to study the average ionization of plasma because the spectrum depends upon the abundance of ions from each charge state which is itself a function of the plasma temperature and density. Mid-Z tracers are used in Inertial Confinement Fusion (ICF) experiments[18] as well as in the production of efficient sources of X-rays,[19] in tokomak diagnostics,[20] and in astrophysics.[21–25] In addition, recent astronomical research[26] shows the presence of Cu ions in dwarf stars.

In the recent past, various efforts have been made to study the L-shell spectroscopy of mid-Z elements, such as line identification from L-Shell copper ions.[12,24,27–33] However, the L-shell spectroscopy of Cu is still not fully understood. In this paper, analysis of the L-shell spectrum of a laser-produced Cu plasma in the wavelength range of 7.5–9.5 Å is performed. The transition wavelengths, transition probabilities, and oscillator strengths of experimentally observed lines are calculated using a Multi-configuration Dirac-Fock (MCDF) method. In this computation, the contribution of relativistic corrections such as two-body Breit corrections and QED corrections due to vacuum polarization and self-energy has also been considered. FLYCHK simulations are used to analyze the distribution of various charge states of Copper and to find the temperature and density of the plasma. Moreover, the effect of opacity on charge state distributions of ions is also studied.

II. EXPERIMENTAL PROCEDURE

The experiment was carried out using an Nd: Glass laser with an output energy of 15 J per pulse with a pulse duration of 500 ps. The laser was focused onto a Cu slab to a spot size of 100 μm using an f/5 lens, yielding intensities up to 4×10^{14} W/cm^2. The experimental chamber was evacuated to a pressure of 4×10^{-5} mbar. An X-ray crystal spectrometer, made up of a Thallium Acid Phthalate (TAP) crystal placed at 45° with respect to the laser axis, was used for the line-emission studies in the spectral range of 7.9–9.5 Å. Two stacked aluminized polycarbonate foils (Alexander Vacuum Research, Inc., trade name: B-10) having a 1/e cut-off of 0.9 keV were used to prevent the scattered visible light from entering the plasma chamber. The TAP crystal spectrally resolves X-ray emission from the laser produced plasma. The reflected X-rays were detected using an X-ray CCD camera (Model VISION 4M, from Rigaku innovative) which has a resolution of 25 mÅ. The schematic of the crystal spectrometer along with the experimental setup is shown in Fig. 1. A sample image of a recorded X-ray spectrum is also shown in Fig. 1.

III. RESULTS AND DISCUSSION

The experimental spectrum consists of transitions corresponding to Oxygen (O–) (Cu XXII), Fluorine (F–) (Cu-XXI), and Neon (Ne–) (Cu-XX) ions. The formation of these multiply charged ions takes place via collision of free electrons with atoms. The highest charge state of Cu in the present experiment

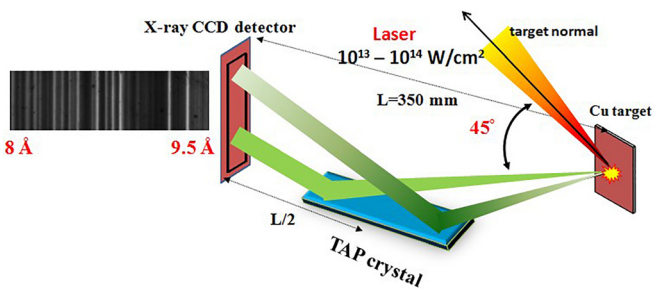

FIG. 1. Schematic of the experimental setup.

is O-like with an ionization potential of 1.9 keV followed by F-like (1.8 keV) and Ne-like (1.69 keV). The Ne-like ions are easy to produce due to the low energy requirement and the closed shell ground configuration in these ions. The shell configuration of Ne-like ions is $1s^2 2s^k 2p^l$ (k = 1, 2; l = 1–6). There are in total seven Rydberg series of dipole transitions from $2s^2 2p^6$–$2s^2 2p^5 nl'$ and $2s^2 2p^6$–$2s2p^6 nl'$. A standard notation for Ne-like lines is followed as provided in the literature[34] nA: 2s-np$_{3/2}$, nB: 2s-np$_{1/2}$, nC: 2p$_{1/2}$-nd$_{3/2}$, nD: 2p$_{3/2}$-nd$_{5/2}$, nE: 2p$_{3/2}$-nd$_{3/2}$, nF: 2p$_{1/2}$-ns, and nG: 2p$_{3/2}$-ns. The procedure followed for the identification of lines and calibration of wavelength is discussed below.

First, identification of the wavelength of the spectral lines is carried out by ray-tracing, considering the location of the crystal and the detector in addition to the dispersion curve of the crystal. Then, the dispersion curve of the crystal is coupled with the two most intense lines of Ne-like (2P-4d) 4C and Ne-like (2p-4d) 2D, which results in a spectrum with an error of 25 mÅ. Further identification is carried out using calculations performed with the General Purpose Relativistic Atomic Structure Package (GRASP) code of Grant *et al.*,[35] which employs the MCDF method. Configuration interaction has been included for O-like, F-like, and Ne-like Cu. Similar calculations have also been performed using the fully relativistic flexible atomic code (FAC). Transition wavelength, oscillator strength, transition probabilities, and line strength are reported for electric dipole (E1), electric quadrupole (E2), magnetic dipole (M1), and magnetic quadrupole (M2) transitions from the ground level. First, for the validation of our code, we match our generated data for some very well-known materials such as the Aluminum and Silicon K-shell spectrum and data available in the literature. Then, we use the same model for our calculation of the spectral lines of Ne-, F-, O-, and Na-like ions. Here, we found some new transitions in both the measured spectra and the calculation, which are not reported earlier and may be useful for plasma parameter estimation.

We compared our calculated results with the available data in the literature. The calculated results are found to be in close agreement with previous results. Furthermore, we predict some new atomic data which may be important for plasma diagnostics.

For Ne-like Cu, in our MCDF calculations, we have included 51 configurations, $2s^2 2p^6$, $2s^2 2p^5 3l$ ($l = 0$–2), $2s2p^6\ 3l$ ($l = 0$–2), $2s2p^6\ 4l$ ($l = 0$–3), $2s^2 2p^5 4l$ ($l = 0$–3), $2s^2 2p^5 5l$ ($l = 0$–3), $2s2p^6 5l$ ($l = 0$–3), $2s^2 2p^5 6l$ ($l = 0$–3), $2s2p^6\ 6l$ ($l = 0$–3), $2s^2 2p^5 7l$ ($l = 0$–3), $2s2p^6 7l$ ($l = 0$–3), $2s^2 2p^4 3s^2$, $2s^2 2p^4 3p^2$, $2s^2 2p^4 3d^2$, $2s2p^5 3s^2$, $2s2p^5 3p^2$, $2s2p^5 3d^2$, $2s^2 2p^4 3s3p$, $2s^2 2p^4 3p3d$, $2s^2 2p^4 3s3d$, $2s2p^5 3s3p$, $2s2p^5 3p3d$, and $2s2p^5 3s3d$, which give rise to 1016 fine structural levels. We mainly focus on one electron excitation by taking 39 configurations of single excitation due to negligible contributions of two or more electron excitations on energy levels and radiative rates.

For F-like Cu, in our MCDF calculations, we have included 27 configurations, $2s^2 2p^5$, $2s2p^6$, $2s^2 2p^4 3l$ ($l = 0$–2), $2s2p^5 3l$ ($l = 0$–2), $2p^6\ 3l$ ($l = 0$–2), $2s^2 2p^4\ 4l$ ($l = 0$–3), $2s2p^5 4l$ ($l = 0$–3), $2s^2 2p^4 5l$ ($l = 0$–3), and $2s2p^5 5l$ ($l = 0$–3), which give rise to 492 fine structural levels.

For O-like Cu, in our MCDF calculations, we have included 54 configurations, $2s^22p^4$, $2s2p^5$,$2p^6$,$2s^22p^33l$ ($l=0$–2), $2s2p^4$ $3l$ ($l=0$–2), $2p^5$ $3l$ ($l=0$–2), $2s^22p^3$ $4l$ ($l=0$–3), $2s2p^44l$ ($l=0$–3), $2p^54l$ ($l=0$–3), $2s^22p^35l$ ($l=0$–4), $2s2p^45l$ ($l=0$–4), $2p^5$ $5l$ ($l=0$–4), $2s^22p^36l$ ($l=0$–4), $2s2p^46l$ ($l=0$–4), and $2p^5$ $6l$ ($l=0$–4), which give rise to 1434 fine structural levels. In our calculations, we have also included the contribution of relativistic corrections such as two-body Breit corrections and QED corrections due to vacuum polarization and self-energy.

For Na-like Cu, in our MCDF calculations, we have included 39 configurations, $2s^22p^63l$ ($l=0$–2), $2s^22p^6$ $4l$ ($l=0$–3), $2s^22p^65l$ ($l=0$–4), $2s^22p^66l$ ($l=0$–4), $2s^22p^67l$ ($l=0$–4), $2s^22p^68l$ ($l=0$–4), and $2s^22p^53l4l'$ ($l=0$–2, $l'=0$–3), which give rise to 619 fine structural levels. In our calculations, we have also included the contribution of relativistic corrections such as two-body Breit corrections and QED corrections due to vacuum polarization and self-energy.

The transition wavelength, transition rates, and oscillator strengths are calculated. The details of the calculated lines (wavelength, transition rates, and oscillator strength) for Ne-like, O-like, F-like, and Na-like Cu transitions are provided in Tables I, II, III, and IV, respectively. For F-like transitions, the configuration details are given in Table V. The wavelength and relative transition rates obtained for different charge states, without considering the ion charge-state populations, are shown in Fig. 2(a) overlaid with the experimentally measured spectrum. All the identified lines are labeled in Fig. 2(b).

Most of the transition lines in the wavelength range under consideration belong to the 2p-nd transition giving rise to nC and nD pairs and the transitions from the 2p-ns and 2s-nd (n = 4–6) levels. The high energy spectral lines are associated with the transition to a $2p_{1/2}$ vacancy in the L-shell and the lower energy spectra result from transitions to fill the $2p_{3/2}$ vacancy.

A. Determination of plasma parameters

These highly charged ions are produced via various ionization processes such as photo-ionization, collisional-ionization, and auto-ionization. The main recombination processes include radiative recombination, three body recombination, and dielectronic recombination. The dominance of collisional or radiative processes decides whether plasma is in complete thermal equilibrium (CTE), local thermal equilibrium (LTE), or collisional radiative (CRE) equilibrium.[36] This in turn depends upon the temperature and density ranges present in the plasma. The knowledge of the equilibrium state facilitates the interpretation of spectroscopic data to uncover the charge state distribution and populations of the excited states.

CTE is not possible in lab environments due to the escape of radiation from the plasma. LTE occurs when the collision time between electrons and ions is short relative to that for other processes taking place in plasma. If LTE is present, then the temperature can be determined easily by the Boltzmann plot method.[37] The collisional radiative equilibrium is non-LTE in the sense that for this to occur, both collisions and radiation must play dominant roles. The solution of this equilibrium lies in solving the rate equations taking care of rates of all collisional and radiative excitation and de-excitation processes.

The validity of applying the LTE equilibrium approximation can be checked by applying the Mc Whirter criterion[38] given by

$$n_e \geq 1.6 \times 10^{12} T^{1/2} (\Delta E)^3, \quad (1)$$

where n_e is the electron density, T is the plasma temperature, and ΔE is the largest electronic transition. In our case, for plasma temperatures greater than 50 eV, the minimum density should be greater than $10^{22}/cm^3$, for the plasma to be in LTE. The required value is greater than our critical density value. Therefore, we can say that our plasma is not in LTE. We used the CRE based code FLYCHK[39] for the determination of plasma temperature and density, and the detailed procedure is provided below. In FLYCHK, opacity effects are included by solving radiative transport equations for optically thick plasmas.

In the spectrum shown in Fig. 2, at a laser intensity of 1.3×10^{14} W/cm^2, the identified lines belong to Ne-, F-, and O-like copper ions. The intensity of Ne-like lines is higher than that of the F-like lines, which indicates that the Ne-like ions are the dominant species. The experimentally observed spectral lines

TABLE I. Calculated wavelength, transition rates, and oscillator strengths of Ne-like transitions along with the corresponding configurations.

Notation	Lower level (i)	Upper level (j)	λ (in Å) (MCDF)	A_{ji} (s^{-1}) (MCDF)	f_{ij} (MCDF)	S_{ij} (a.u.) (MCDF)	Type	λ_{FLYCHK} (Å)
4D	$2s^22p^6{}^1S_0$	$2s^22p^54d\ {}^1P_1$	9.2443	1.12×10^{13}	4.30×10^{-1}	1.31×10^{-2}	E1	9.2673
4C	$2s^22p^6{}^1S_0$	$2s^22p^54d\ {}^3D_1$	9.1144	1.06×10^{13}	3.97×10^{-1}	1.19×10^{-2}	E1	9.1254
	$2s^22p^6{}^1S_0$	$2s^22p^55s\ {}^1P_1$	8.5723	3.89×10^{11}	1.29×10^{-2}	3.63×10^{-4}	E1	
	$2s^22p^6{}^1S_0$	$2s^22p^55d\ {}^3P_1$	8.4708	7.86×10^{10}	2.54×10^{-3}	7.08×10^{-5}	E1	
5D	$2s^22p^6{}^1S_0$	$2s^22p^55d\ {}^1P_1$	8.4562	6.14×10^{12}	1.97×10^{-1}	5.50×10^{-3}	E1	
	$2s^22p^6{}^1S_0$	$2s^22p^55s^3P_1$	8.4507	1.23×10^{12}	3.96×10^{-2}	1.10×10^{-3}	E1	
4A, 4B	$2s^22p^6{}^1S_0$	$2s2p^64p\ {}^3P_1$	8.3899	1.12×10^{12}	3.55×10^{-2}	9.80×10^{-4}	E1	8.3823
	$2s^22p^6{}^1S_0$	$2s2p^64p\ {}^1P_1$	8.3763	3.14×10^{12}	9.91×10^{-2}	2.73×10^{-3}	E1	
5C	$2s^22p^6{}^1S_0$	$2s^22p^55d\ {}^3D_1$	8.3419	3.98×10^{12}	1.24×10^{-1}	3.42×10^{-3}	E1	8.344
	$2s^22p^6{}^1S_0$	$2s^22p^56s\ {}^1P_1$	8.1413	2.02×10^{11}	6.03×10^{-3}	1.62×10^{-4}	E1	
	$2s^22p^6{}^1S_0$	$2s^22p^56D^3P_1$	8.0893	3.26×10^{10}	9.60×10^{-4}	2.56×10^{-5}	E1	
6D	$2s^22p^6{}^1S_0$	$2s^22p^56D^1P_1$	8.0809	4.51×10^{12}	1.32×10^{-1}	3.52×10^{-3}	E1	8.0844
6F	$2s^22p^6{}^1S_0$	$2s^22p^56S^3P_1$	8.032	6.84×10^{10}	1.99×10^{-3}	5.25×10^{-5}	E1	
6C	$2s^22p^6{}^1S_0$	$2s^22p^56D^3D_1$	7.9761	2.56×10^{12}	7.32×10^{-2}	1.92×10^{-3}	E1	7.975

TABLE II. Calculated wavelength, transition rates, and oscillator strengths of O-like transitions along with the corresponding configurations.

Transition					
Lower level (i)	Upper level (j)	λ (in Å)	A_{ji} (s^{-1})	f_{ij}	S_{ij} (a.u.)
$2s^22p^4({}^3P)_2$	$2s^22p^3\,({}^4S)4d\,{}^5D^o_1$	8.3059	4.192×10^{11}	2.601×10^{-3}	3.557×10^{-4}
$2s^22p^4({}^3P)_2$	$2s^22p^3\,({}^4S)4d\,{}^3D^o_2$	8.2904	2.819×10^{12}	2.905×10^{-2}	3.964×10^{-3}
$2s^22p^4({}^3P)_2$	$2s^22p^3\,({}^4S)4d\,{}^3D^o_1$	8.2793	3.002×10^{11}	1.851×10^{-3}	2.522×10^{-4}
$2s^22p^4({}^3P)_2$	$2s^22p^3\,({}^4S)4d\,{}^3D^o_3$	8.2782	1.002×10^{13}	1.441×10^{-1}	1.963×10^{-2}
$2s^22p^4({}^3P)_0$	$2s^22p^3\,({}^2D)4d\,{}^3D^o_1$	8.2540	8.167×10^{11}	2.502×10^{-2}	6.800×10^{-4}
$2s^22p^4({}^3P)_0$	$2s^22p^3\,({}^2D)4d\,{}^3P^o_1$	8.2352	1.196×10^{12}	3.649×10^{-2}	9.893×10^{-4}
$2s^22p^4({}^3P)_0$	$2s^22p^3\,({}^2D)4d\,{}^1P^o_1$	8.2034	3.572×10^{10}	1.081×10^{-3}	2.920×10^{-5}
$2s^22p^4({}^3P)_1$	$2s^22p^3\,({}^4S)4d^3D^o_3$	8.2875	7.137×10^{9}	7.349×10^{-5}	6.015×10^{-6}
$2s^22p^4({}^3P)_1$	$2s^22p^3\,({}^2D)4d\,{}^3F^o_2$	8.2878	6.513×10^{11}	1.118×10^{-2}	9.150×10^{-4}
$2s^22p^4({}^3P)_1$	$2s^22p^3\,({}^2D)4d\,{}^1S^o_0$	8.2848	6.691×10^{11}	2.295×10^{-3}	1.878×10^{-4}
$2s^22p^4({}^3P)_1$	$2s^22p^3\,({}^2D)4d\,{}^1P^o_1$	8.2686	4.147×10^{12}	4.251×10^{-2}	3.471×10^{-3}
$2s^22p^4({}^3P)_1$	$2s^22p^3\,({}^2D)4d\,{}^3D^o_2$	8.2690	5.075×10^{12}	8.670×10^{-2}	7.081×10^{-3}
$2s^22p^4({}^3P)_1$	$2s^22p^3\,({}^2D)4d\,{}^3P^o_0$	8.2400	4.412×10^{12}	1.497×10^{-2}	1.218×10^{-3}
$2s^22p^4({}^3P)_1$	$2s^22p^3\,({}^2D)4d\,{}^3P^o_2$	8.2377	4.716×10^{11}	7.995×10^{-3}	6.505×10^{-4}
$2s^22p^4({}^3P)_1$	$2s^22p^3\,({}^2D)4d\,{}^3F^o_2$	8.2365	2.960×10^{12}	3.010×10^{-2}	2.449×10^{-3}
$2s^22p^4({}^3P)_1$	$2s^22p^3\,({}^2D)4d\,{}^3S^o_1$	8.2290	7.566×10^{11}	7.681×10^{-3}	6.243×10^{-4}
$2s^22p^4({}^3P)_1$	$2s^22p^3\,({}^2D)4d\,{}^1D^o_2$	8.2256	9.513×10^{11}	1.608×10^{-2}	1.307×10^{-3}
$2s^22p^4({}^1D)_2$	$2s^22p^3\,({}^2D)4d\,{}^3P^o_2$	8.2984	2.688×10^{9}	2.775×10^{-5}	3.791×10^{-6}
$2s^22p^4({}^1D)_2$	$2s^22p^3\,({}^2D)4d\,{}^1P^o_1$	8.2972	8.351×10^{11}	5.172×10^{-3}	7.063×10^{-4}
$2s^22p^4({}^1D)_2$	$2s^22p^3\,({}^2D)4d\,{}^3S^o_1$	8.2895	3.687×10^{12}	2.279×10^{-2}	3.110×10^{-3}
$2s^22p^4({}^1D)_2$	$2s^22p^3\,({}^2D)4d\,{}^1D^o_2$	8.2861	8.344×10^{12}	8.589×10^{-2}	1.171×10^{-2}
$2s^22p^4({}^1D)_2$	$2s^22p^3\,({}^2D)4d\,{}^1F^o_3$	8.2836	9.957×10^{12}	1.434×10^{-1}	1.955×10^{-2}
$2s^22p^4({}^1D)_2$	$2s^22p^3\,({}^2P)4d\,{}^3F^o_2$	8.2430	1.309×10^{12}	1.333×10^{-2}	1.809×10^{-3}
$2s^22p^4({}^1D)_2$	$2s^22p^3\,({}^2P)4d\,{}^3P^o_2$	8.2363	8.564×10^{11}	8.709×10^{-3}	1.181×10^{-3}
$2s^22p^4({}^1D)_2$	$2s^22p^3\,({}^2P)4d\,{}^3F^o_3$	8.2348	3.616×10^{12}	5.147×10^{-2}	6.977×10^{-3}
$2s^22p^4({}^1D)_2$	$2s^22p^3\,({}^2P)4d\,{}^3D^o_1$	8.2276	2.239×10^{11}	1.364×10^{-3}	1.847×10^{-4}
$2s^22p^4({}^1S)_0$	$2s^22p^3\,({}^2P)4d\,{}^3P^o_1$	8.3074	6.048×10^{11}	1.877×10^{-2}	5.134×10^{-4}
$2s^22p^4({}^1S)_0$	$2s^22p^3\,({}^2P)4d\,{}^1P^o_1$	8.2791	1.639×10^{13}	5.053×10^{-1}	1.377×10^{-2}
$2s2p^5({}^3P)^o_2$	$2s2p^4({}^2D)4d\,{}^3G_3$	8.2069	8.830×10^{10}	1.248×10^{-3}	1.686×10^{-4}
$2s2p^5({}^3P)^o_1$	$2s2p^4({}^2D)4d\,{}^3F_2$	8.2635	5.205×10^{10}	8.880×10^{-4}	7.247×10^{-5}
$2s2p^5({}^3P)^o_1$	$2s2p^4({}^2D)4d\,{}^3D_1$	8.2602	3.602×10^{12}	3.684×10^{-2}	3.006×10^{-3}
$2s2p^5({}^3P)^o_1$	$2s2p^4({}^2D)4d\,{}^3D_2$	8.2551	4.838×10^{12}	8.238×10^{-2}	6.716×10^{-3}
$2s2p^5({}^3P)^o_1$	$2s2p^4({}^2D)4d\,{}^3P_1$	8.2536	2.240×10^{12}	2.287×10^{-2}	1.865×10^{-3}
$2s2p^5({}^3P)^o_1$	$2s2p^4({}^2D)4d\,{}^3S_1$	8.2397	1.092×10^{9}	1.111×10^{-5}	9.043×10^{-7}
$2s2p^5({}^3P)^o_1$	$2s2p^4({}^2D)4d\,{}^3P_2$	8.2378	6.660×10^{10}	1.129×10^{-3}	9.188×10^{-5}
$2s2p^5({}^3P)^o_1$	$2s2p^4({}^2D)4d\,{}^1D_2$	8.2260	7.385×10^{11}	1.249×10^{-2}	1.014×10^{-3}
$2s2p^5({}^3P)^o_1$	$2s2p^4({}^2D)4d\,{}^1P_1$	8.2247	1.734×10^{12}	1.759×10^{-2}	1.428×10^{-3}
$2s2p^5({}^3P)^o_1$	$2s2p^4({}^2D)4d\,{}^1S_0$	8.2210	2.454×10^{12}	8.288×10^{-3}	6.729×10^{-4}
$2s2p^5({}^3P)^o_0$	$2s2p^4({}^2D)4d\,{}^3P_1$	8.3086	8.701×10^{12}	2.701×10^{-1}	7.389×10^{-3}
$2s2p^5({}^3P)^o_0$	$2s2p^4({}^2D)4d\,{}^3S_1$	8.2945	2.293×10^{11}	7.094×10^{-3}	1.937×10^{-4}
$2s2p^5({}^3P)^o_0$	$2s2p^4({}^2D)4d\,{}^1P_1$	8.2793	2.470×10^{11}	7.613×10^{-3}	2.075×10^{-4}
$2s2p^5({}^3P)^o_0$	$2s2p^4({}^2S)4d\,{}^3D_1$	8.2048	3.162×10^{11}	9.575×10^{-3}	2.586×10^{-4}
$2s2p^5({}^1P)^o_1$	$2s2p^4({}^2P)4d\,{}^1P_1$	8.3052	5.363×10^{12}	5.546×10^{-2}	4.549×10^{-3}
$2s2p^5({}^1P)^o_1$	$2s2p^4({}^2P)4d\,{}^1D_2$	8.3046	1.026×10^{13}	1.767×10^{-1}	1.450×10^{-2}
$2s2p^5({}^1P)^o_1$	$2s2p^4({}^2P)4d\,{}^3D_1$	8.2150	4.069×10^{12}	4.117×10^{-2}	3.340×10^{-3}
$2s2p^5({}^1P)^o_1$	$2s2p^4({}^2P)4d\,{}^3P_2$	8.2145	5.453×10^{11}	9.194×10^{-3}	7.459×10^{-4}
$2s2p^5({}^1P)^o_1$	$2s2p^4({}^2P)4d\,{}^3D_2$	8.2094	7.559×10^{12}	1.273×10^{-1}	1.032×10^{-2}

consist of 2p–4d, 2p–5d, and 2p–6d transitions. These lines exist in pairs corresponding to resonance lines (nC) with transition $2s^22p^5nd_{3/2}\,{}^1P_1$–$2s^22p^6\,{}^1S_0$ and intercombination (IC) (nD) for $2s^22p^5nd_{1/2}\,{}^3D_1$–$2s^22p^6\,{}^1S_0$ (n = 4–6 in our case). The ratio nC/nD is a strong function of the ion abundance which is a function of plasma temperature and density.[40] Our experimentally observed spectrum is time integrated, but it should be borne in mind that the plasma has strong temperature and density gradients which are a function of time. The Ne-like spectra of Cu dominate for a range of temperatures and densities.

TABLE III. Calculated wavelength, transition rates, and oscillator strengths of F-like transitions along with the corresponding configurations.

I	J	λ (in Å)	A_{ji} (s^{-1})	f_{ij}	S_{ij} (a.u.)
3	434	8.08	1.75×10^{10}	1.71×10^{-4}	9.12×10^{-6}
3	424	8.08	6.09×10^{7}	1.19×10^{-6}	6.33×10^{-8}
2	253	8.08	9.10×10^{11}	1.78×10^{-2}	9.47×10^{-4}
2	246	8.08	9.51×10^{11}	9.31×10^{-3}	4.95×10^{-4}
1	209	8.09	3.27×10^{12}	3.20×10^{-2}	3.41×10^{-3}
3	410	8.09	7.95×10^{12}	7.79×10^{-2}	4.15×10^{-3}
1	208	8.09	1.39×10^{12}	2.05×10^{-2}	2.18×10^{-3}
2	242	8.09	3.71×10^{11}	7.28×10^{-3}	3.88×10^{-4}
2	241	8.09	1.11×10^{12}	1.09×10^{-2}	5.83×10^{-4}
2	240	8.09	3.72×10^{11}	7.31×10^{-3}	3.89×10^{-4}
3	407	8.09	3.28×10^{12}	6.44×10^{-2}	3.43×10^{-3}
1	182	8.59	5.30×10^{12}	8.81×10^{-2}	9.97×10^{-3}
3	371	8.59	7.30×10^{11}	1.62×10^{-2}	9.15×10^{-4}
3	370	8.60	7.27×10^{11}	8.05×10^{-3}	4.56×10^{-4}
1	180	8.60	7.49×10^{12}	8.30×10^{-2}	9.40×10^{-3}
1	179	8.60	9.02×10^{12}	5.00×10^{-2}	5.66×10^{-3}
1	178	8.60	4.42×10^{11}	7.35×10^{-3}	8.32×10^{-4}
1	169	8.65	1.63×10^{11}	9.14×10^{-4}	1.04×10^{-4}
1	166	8.65	5.24×10^{11}	5.89×10^{-3}	6.71×10^{-4}
1	165	8.66	4.38×10^{12}	7.39×10^{-2}	8.43×10^{-3}
1	163	8.66	2.09×10^{12}	3.53×10^{-2}	4.03×10^{-3}
1	164	8.67	4.91×10^{11}	8.29×10^{-3}	9.46×10^{-4}
1	162	8.67	1.04×10^{12}	1.18×10^{-2}	1.34×10^{-3}
1	160	8.67	2.64×10^{11}	2.98×10^{-3}	3.40×10^{-4}
1	159	8.68	2.70×10^{11}	1.52×10^{-3}	1.74×10^{-4}
3	351	8.70	1.98×10^{10}	4.50×10^{-4}	2.58×10^{-5}
3	346	8.70	5.01×10^{8}	1.14×10^{-5}	6.51×10^{-7}
3	345	8.70	1.98×10^{10}	2.24×10^{-4}	1.28×10^{-5}
1	155	8.70	1.93×10^{12}	3.28×10^{-2}	3.76×10^{-3}
2	184	8.71	1.45×10^{13}	1.65×10^{-1}	9.47×10^{-3}
1	152	8.71	7.48×10^{11}	8.51×10^{-3}	9.75×10^{-4}
2	183	8.71	8.77×10^{12}	1.99×10^{-1}	1.14×10^{-2}
2	180	8.72	1.90×10^{12}	4.34×10^{-2}	2.49×10^{-3}
2	179	8.72	6.49×10^{11}	7.41×10^{-3}	4.25×10^{-4}
1	140	8.76	8.29×10^{12}	1.43×10^{-1}	1.65×10^{-2}
3	328	8.76	1.69×10^{12}	3.88×10^{-2}	2.24×10^{-3}
1	139	8.76	7.21×10^{12}	8.30×10^{-2}	9.58×10^{-3}
3	320	8.76	5.94×10^{7}	6.84×10^{-7}	3.95×10^{-8}
3	319	8.77	1.32×10^{12}	3.05×10^{-2}	1.76×10^{-3}
1	136	8.77	3.32×10^{12}	1.92×10^{-2}	2.22×10^{-3}
3	318	8.77	3.69×10^{12}	8.52×10^{-2}	4.92×10^{-3}
3	316	8.78	1.27×10^{8}	2.93×10^{-6}	1.69×10^{-7}
2	169	8.78	8.99×10^{11}	1.04×10^{-2}	6.01×10^{-4}
2	166	8.78	4.48×10^{12}	1.04×10^{-1}	5.99×10^{-3}
1	131	8.79	3.03×10^{10}	1.75×10^{-4}	2.03×10^{-5}
3	305	8.79	4.01×10^{10}	4.64×10^{-4}	2.69×10^{-5}
1	130	8.79	3.16×10^{9}	3.66×10^{-5}	4.23×10^{-6}
1	128	8.79	3.22×10^{9}	5.60×10^{-5}	6.48×10^{-6}
2	160	8.80	2.83×10^{10}	6.58×10^{-4}	3.81×10^{-5}
2	162	8.80	3.46×10^{11}	8.04×10^{-3}	4.66×10^{-4}
3	297	8.80	2.90×10^{11}	6.74×10^{-3}	3.90×10^{-4}
2	159	8.80	3.89×10^{11}	4.52×10^{-3}	2.62×10^{-4}
1	126	8.81	2.77×10^{10}	3.23×10^{-4}	3.75×10^{-5}
1	125	8.81	8.54×10^{11}	1.49×10^{-2}	1.73×10^{-3}
3	293	8.83	5.72×10^{12}	1.34×10^{-1}	7.76×10^{-3}
3	289	8.84	2.35×10^{12}	2.75×10^{-2}	1.60×10^{-3}
2	152	8.84	7.94×10^{10}	1.86×10^{-3}	1.08×10^{-4}
3	287	8.84	1.23×10^{12}	2.89×10^{-2}	1.68×10^{-3}
3	285	8.84	4.73×10^{11}	5.54×10^{-3}	3.22×10^{-4}
3	283	8.84	1.28×10^{11}	3.00×10^{-3}	1.74×10^{-4}
3	282	8.85	1.40×10^{11}	3.28×10^{-3}	1.91×10^{-4}
3	277	8.85	7.27×10^{10}	8.54×10^{-4}	4.98×10^{-5}
3	266	8.88	1.92×10^{9}	4.53×10^{-5}	2.65×10^{-6}
3	269	8.88	5.86×10^{12}	6.92×10^{-2}	4.05×10^{-3}
1	121	8.88	4.84×10^{11}	2.86×10^{-3}	3.34×10^{-4}
3	264	8.88	8.37×10^{11}	1.98×10^{-2}	1.16×10^{-3}
3	257	8.88	3.46×10^{9}	8.19×10^{-5}	4.79×10^{-6}
3	247	8.88	2.43×10^{12}	2.88×10^{-2}	1.68×10^{-3}
1	120	8.88	3.07×10^{11}	3.63×10^{-3}	4.25×10^{-4}
3	245	8.89	3.56×10^{12}	4.22×10^{-2}	2.47×10^{-3}
2	139	8.89	3.80×10^{11}	9.01×10^{-3}	5.28×10^{-4}
3	243	8.90	3.29×10^{12}	7.82×10^{-2}	4.58×10^{-3}
2	136	8.90	2.04×10^{11}	2.42×10^{-3}	1.42×10^{-4}
2	131	8.92	1.24×10^{11}	1.48×10^{-3}	8.68×10^{-5}
2	130	8.92	5.71×10^{10}	1.36×10^{-3}	8.00×10^{-5}
1	114	8.92	3.81×10^{11}	2.27×10^{-3}	2.67×10^{-4}
3	226	8.93	2.23×10^{10}	5.32×10^{-4}	3.13×10^{-5}
3	225	8.93	1.14×10^{10}	1.37×10^{-4}	8.05×10^{-6}
2	126	8.94	6.65×10^{11}	1.60×10^{-2}	9.40×10^{-4}
3	221	8.95	4.53×10^{10}	1.09×10^{-3}	6.41×10^{-5}
3	218	8.96	1.12×10^{10}	1.35×10^{-4}	7.95×10^{-6}
3	215	8.97	1.39×10^{6}	3.36×10^{-8}	1.98×10^{-9}
3	213	9.00	6.07×10^{11}	7.36×10^{-3}	4.36×10^{-4}
1	111	9.00	1.12×10^{12}	1.35×10^{-2}	1.60×10^{-3}
1	110	9.01	6.73×10^{10}	1.23×10^{-3}	1.46×10^{-4}
2	121	9.01	7.52×10^{11}	9.15×10^{-3}	5.43×10^{-4}

To get a more accurate temperature and density for the most strongly radiating portion of the plasma generated at 1.4×10^{14} W/cm^2, we compare 4C and 4D lines and the ratio of 4D with the Na-like IS satellite with the synthetic spectra generated by the FLYCHK code. The Na-like satellite lines originated from doubly excited Ne-like ions are observed and are reported by a few authors[41–43] with very high precision. The energy level scheme for Ne-like and Na-like Cu is shown in Fig. 3(a). The 4D resonance line consists of a Na-like satellite line whose identification is provided in Ref. 42 with accuracy on the order of 0.001 Å. In Ref. 42, 4C and 4D lines along with several Na-like satellite transitions are given. Due to the comparatively low resolution of our crystal spectrometer, we are not able to distinguish all IS (inner shell) satellite lines. In Fig. 3(b), the experimentally observed satellite transitions are plotted. These consist of transitions from $3s\text{-}4d_{3/2}$, $4p_{3/2}$, $3p_{3/2}\text{–}4d_{5/2,3/2}$,$4d_{3/2}\text{–}3s_{1/2}$, $3p_{1/2}$, and $3d_{3/2,5/2}$.This satellite emission is also shown by FLYCHK. To match this experimental spectrum, we have run simulations over a wide range of temperatures and densities. Temperature is varied from 100 eV to 400 eV, and the density is varied from 1×10^{20} cm^{-3} to 1×10^{21} cm^{-3}. The effect of varying temperature and density on the ratios (4C/4D and Na-like satellite/4D) is

TABLE IV. Calculated wavelength, transition rates, oscillator strengths, and line strengths of Na-like transitions along with the corresponding configurations.

Transitions					
I	J	λ (in Å)	A_{ji} (in s^{-1})	f_{ij}	S_{ij} (in a.u.)
$2s^22p^6\ 3s\ ^2S_{1/2}$	$2p^53p\ (^1D)\ 4p\ ^2D^o_{3/2}$	9.338	4.4701×10^{10}	1.1687×10^{-3}	7.1853×10^{-5}
$2s^22p^6\ 3s\ ^2S_{1/2}$	$2p^53s\ (^3P)\ 4d\ ^4F^o_{3/2}$	9.338	2.1180×10^{11}	5.5376×10^{-3}	3.4047×10^{-4}
$2s^22p^6\ 3s\ ^2S_{1/2}$	$2p^53s\ (^1P)\ 4d\ ^2P^o_{3/2}$	9.324	7.3068×10^{10}	9.5227×10^{-4}	5.8459×10^{-5}
$2s^22p^6\ 3s\ ^2S_{1/2}$	$2p^53p\ (^1P)\ 4p\ ^2S^o_{1/2}$	9.327	1.1345×10^{11}	2.9590×10^{-3}	1.8171×10^{-4}
$2s^22p^6\ 3s\ ^2S_{1/2}$	$2p^53p\ (^1P)\ 4p\ ^2D^o_{3/2}$	9.318	1.1527×10^{12}	3.0006×10^{-2}	1.8408×10^{-3}
$2s^22p^6\ 3s\ ^2S_{1/2}$	$2p^53p\ (^1P)\ 4p\ ^2P^o_{3/2}$	9.314	5.6739×10^{12}	1.4760×10^{-1}	9.0517×10^{-3}
$2s^22p^6\ 3s\ ^2S_{1/2}$	$2p^53s\ (^3P)\ 4d\ ^2P^o_{3/2}$	9.311	1.5616×10^{12}	4.0591×10^{-2}	2.4884×10^{-3}
$2s^22p^6\ 3s\ ^2S_{1/2}$	$2p^53s\ (^1P)\ 4d\ ^2P^o_{1/2}$	9.313	9.0861×10^{12}	1.1813×10^{-1}	7.2433×10^{-3}
$2s^22p^6\ 3s\ ^2S_{1/2}$	$2p^53p\ (^3S)\ 4p\ ^2P^o_{1/2}$	9.307	7.1495×10^{10}	9.2834×10^{-4}	5.6886×10^{-5}
$2s^22p^6\ 3s\ ^2S_{1/2}$	$2p^53p\ (^1P)\ 4p\ ^2P^o_{1/2}$	9.301	1.2043×10^{11}	1.5620×10^{-3}	9.5661×10^{-5}
$2s^22p^6\ 3s\ ^2S_{1/2}$	$2p^53p\ (^3P)\ 4p\ ^4P^o_{3/2}$	9.300	1.6389×10^{11}	4.2500×10^{-3}	2.6023×10^{-4}
$2s^22p^6\ 3s\ ^2S_{1/2}$	$2p^53p\ (^3P)\ 4p\ ^4D^o_{7/2}$	9.292	7.5641×10^{10}	9.7909×10^{-4}	5.9901×10^{-5}
$2s^22p^6\ 3s\ ^2S_{1/2}$	$2p^53p\ (^3D)\ 4s\ ^2D_{3/2}$	9.268	3.4377×10^{10}	8.8541×10^{-4}	5.4031×10^{-5}
$2s^22p^6\ 3s\ ^2S_{1/2}$	$2p^53p\ (^3P)\ 4p\ ^2P^o_{3/2}$	9.255	9.5897×10^{9}	2.4631×10^{-4}	1.5010×10^{-5}
$2s^22p^6\ 3p\ ^2P^o_{1/2}$	$2p^53p\ (^3D)\ 4d\ ^4F_{3/2}$	9.337	5.7154×10^{12}	1.4940×10^{-1}	9.1844×10^{-3}
$2s^22p^6\ 3p\ ^2P^o_{1/2}$	$2p^53p\ (^1P)\ 4d\ ^2P_{1/2}$	9.329	8.2166×10^{12}	1.0719×10^{-1}	6.5838×10^{-3}
$2s^22p^6\ 3p\ ^2P^o_{1/2}$	$2p^53p\ (^3P)\ 4d\ ^2P_{3/2}$	9.309	3.3101×10^{11}	8.5998×10^{-3}	5.2707×10^{-4}
$2s^22p^6\ 3p\ ^2P^o_{1/2}$	$2p^53p\ (^1D)\ 4d\ ^2G_{7/2}$	9.301	7.5888×10^{10}	1.9685×10^{-3}	1.2055×10^{-4}
$2s^22p^6\ 3p\ ^2P^o_{1/2}$	$2p^53p\ (^3P)\ 4d\ ^4D_{1/2}$	9.299	5.5562×10^{11}	7.2022×10^{-3}	4.4094×10^{-4}
$2s^22p^6\ 3p\ ^2P^o_{1/2}$	$2p^53p\ (^3P)\ 4d\ ^2D_{3/2}$	9.290	3.5322×10^{10}	9.1399×10^{-4}	5.5905×10^{-5}
$2s^22p^6\ 3p\ ^2P^o_{1/2}$	$2p^53p\ (^3D)\ 4d\ ^2P_{1/2}$	9.287	1.2769×10^{11}	1.6512×10^{-3}	1.0097×10^{-4}
$2s^22p^6\ 3p\ ^2P^o_{1/2}$	$2p^53p\ (^1D)\ 4d\ ^2P_{3/2}$	9.286	4.2848×10^{10}	1.1079×10^{-3}	6.7740×10^{-5}
$2s^22p^6\ 3p\ ^2P^o_{1/2}$	$2p^53d\ (^3P)\ 4p\ ^4D_{1/2}$	9.278	1.7559×10^{11}	2.2660×10^{-3}	1.3843×10^{-4}
$2s^22p^6\ 3p\ ^2P^o_{1/2}$	$2p^53p\ (^3D)\ 4d\ ^4P_{1/2}$	9.274	6.0317×10^{08}	7.7770×10^{-6}	4.7487×10^{-7}
$2s^22p^6\ 3p\ ^2P^o_{1/2}$	$2p^53d\ (^3P)\ 4p\ ^4D_{3/2}$	9.266	6.3656×10^{07}	1.6386×10^{-6}	9.9961×10^{-8}
$2s^22p^6\ 3p\ ^2P^o_{1/2}$	$2p^53d\ (^3P)\ 4p\ ^4P_{1/2}$	9.262	3.1616×10^{09}	4.0656×10^{-5}	2.4792×10^{-6}
$2s^22p^6\ 3p\ ^2P^o_{1/2}$	$2p^53d\ (^3P)\ 4p\ ^4P_{3/2}$	9.257	2.3225×10^{10}	5.9677×10^{-4}	3.6374×10^{-5}
$2s^22p^6\ 3p\ ^2P^o_{1/2}$	$2p^53d\ (^3P)\ 4p\ ^2P_{1/2}$	9.253	2.4053×10^{10}	3.0871×10^{-4}	1.8807×10^{-5}
$2s^22p^6\ 3p\ ^2P^o_{1/2}$	$2p^53d\ (^3D)\ 4p\ ^4D_{3/2}$	9.251	2.1206×10^{10}	5.4414×10^{-4}	3.3143×10^{-5}
$2s^22p^6\ 3p\ ^2P^o_{3/2}$	$2p^53p\ (^1D)\ 4d\ ^2G_{7/2}$	9.333	8.3347×10^{09}	1.0883×10^{-4}	1.3374×10^{-5}
$2s^22p^6\ 3p\ ^2P^o_{3/2}$	$2p^53p\ (^3P)\ 4d\ ^4D_{1/2}$	9.330	2.7063×10^{11}	1.7658×10^{-3}	2.1695×10^{-4}
$2s^22p^6\ 3p\ ^2P^o_{3/2}$	$2p^53p\ (^1D)\ 4d\ ^2D_{5/2}$	9.330	3.8666×10^{06}	7.5692×10^{-8}	9.2997×10^{-9}
$2s^22p^6\ 3p\ ^2P^o_{3/2}$	$2p^53p\ (^3P)\ 4d\ ^2D_{3/2}$	9.321	4.9627×10^{12}	6.4639×10^{-2}	7.9340×10^{-3}
$2s^22p^6\ 3p\ ^2P^o_{3/2}$	$2p^53p\ (^3P)\ 4d\ ^2D_{5/2}$	9.320	7.7799×10^{12}	1.5197×10^{-1}	1.8652×10^{-2}
$2s^22p^6\ 3p\ ^2P^o_{3/2}$	$2p^53p\ (^3D)\ 4d\ ^2P_{1/2}$	9.319	5.9580×10^{10}	3.8780×10^{-4}	4.7587×10^{-5}
$2s^22p^6\ 3p\ ^2P^o_{3/2}$	$2p^53p\ (^1D)\ 4d\ ^2P_{3/2}$	9.318	2.0452×10^{12}	2.6619×10^{-2}	3.2661×10^{-3}
$2s^22p^6\ 3p\ ^2P^o_{3/2}$	$2p^53d\ (^3P)\ 4p\ ^4D_{1/2}$	9.309	8.2370×10^{12}	5.3508×10^{-2}	6.5595×10^{-3}
$2s^22p^6\ 3p\ ^2P^o_{3/2}$	$2p^53d\ (^3D)\ 4d\ ^4P_{1/2}$	9.305	6.5583×10^{9}	4.2564×10^{-5}	5.2155×10^{-6}
$2s^22p^6\ 3p\ ^2P^o_{3/2}$	$2p^53d\ (^3P)\ 4p\ ^4D_{3/2}$	9.297	1.5688×10^{8}	2.0327×10^{-6}	2.4884×10^{-7}
$2s^22p^6\ 3p\ ^2P^o_{3/2}$	$2p^53d\ (^3P)\ 4p\ ^4P_{1/2}$	9.293	7.3148×10^{9}	4.7347×10^{-5}	5.7938×10^{-6}
$2s^22p^6\ 3p\ ^2P^o_{3/2}$	$2p^53d\ (^3P)\ 4p\ ^4P_{3/2}$	9.288	8.7983×10^{8}	1.1379×10^{-5}	1.3918×10^{-6}
$2s^22p^6\ 3p\ ^2P^o_{3/2}$	$2p^53d\ (^3P)\ 4p\ ^4D_{5/2}$	9.284	1.1237×10^{10}	2.1781×10^{-4}	2.6629×10^{-5}
$2s^22p^6\ 3p\ ^2P^o_{3/2}$	$2p^53d\ (^3P)\ 4p\ ^2P_{1/2}$	9.284	3.5936×10^{10}	2.3216×10^{-4}	2.8382×10^{-5}
$2s^22p^6\ 3p\ ^2P^o_{3/2}$	$2p^53d\ (^3D)\ 4p\ ^4D_{3/2}$	9.282	9.1824×10^{9}	1.1860×10^{-4}	1.4496×10^{-5}
$2s^22p^6\ 3p\ ^2P^o_{3/2}$	$2p^53d\ (^3F)\ 4p\ ^4F_{7/2}$	9.279	5.7375×10^{10}	1.1109×10^{-3}	1.3575×10^{-4}
$2s^22p^6\ 3p\ ^2P^o_{3/2}$	$2p^53d\ (^3F)\ 4p\ ^4F_{5/2}$	9.274	6.1208×10^{10}	1.1838×10^{-3}	1.4457×10^{-4}
$2s^22p^6\ 3p\ ^2P^o_{3/2}$	$2p^53d\ (^3P)\ 4p\ ^4P_{5/2}$	9.271	8.2346×10^{6}	1.5915×10^{-7}	1.9429×10^{-8}
$2s^22p^6\ 3p\ ^2P^o_{3/2}$	$2p^53d\ (^3F)\ 4p\ ^4F_{9/2}$	9.269	3.1637×10^{8}	4.0745×10^{-6}	4.9730×10^{-7}
$2s^22p^6\ 3p\ ^2P^o_{3/2}$	$2p^53d\ (^1D)\ 4p\ ^2D_{3/2}$	9.266	1.6423×10^{10}	2.1137×10^{-4}	2.5789×10^{-5}
$2s^22p^6\ 3p\ ^2P^o_{3/2}$	$2p^53d\ (^1F)\ 4p\ ^2F_{5/2}$	9.262	3.5491×10^{10}	6.8462×10^{-4}	8.3499×10^{-5}
$2s^22p^6\ 3p\ ^2P^o_{3/2}$	$2p^53d\ (^1D)\ 4p\ ^2F_{5/2}$	9.258	2.3296×10^{9}	4.4902×10^{-5}	5.4743×10^{-6}
$2s^22p^6\ 3p\ ^2P^o_{3/2}$	$2p^53d\ (^3P)\ 4p\ ^2D_{3/2}$	9.251	6.2299×10^{10}	7.9935×10^{-4}	9.7381×10^{-5}
$2s^22p^6\ 3p\ ^2P^o_{3/2}$	$2p^53p\ (^1D)\ 4f\ ^2F^o_{7/2}$	9.249	9.4811×10^{10}	6.0792×10^{-4}	7.4040×10^{-5}
$2s^22p^6\ 3d\ ^2D_{3/2}$	$2p^53d\ (^3P)\ 4d\ ^2F^o_{7/2}$	9.333	2.5352×10^{10}	1.6555×10^{-4}	2.0347×10^{-5}

TABLE IV. (*Continued.*)

Transitions					
I	J	λ (in Å)	A_{ji} (in s^{-1})	f_{ij}	S_{ij} (in a.u.)
$2s^22p^6\ 3d\ ^2D_{3/2}$	$2p^53d\ (^1F)\ 4d\ ^2P^o_{3/2}$	9.330	8.4570×10^{10}	1.1036×10^{-3}	1.3559×10^{-4}
$2s^22p^6\ 3d\ ^2D_{3/2}$	$2p^53d\ (^3D)\ 4d\ ^4S^o_{3/2}$	9.328	4.3146×10^{9}	5.6281×10^{-5}	6.9131×10^{-6}
$2s^22p^6\ 3d\ ^2D_{3/2}$	$2p^53d\ (^1F)\ 4d\ ^2D^o_{5/2}$	9.324	4.3145×10^{9}	8.4355×10^{-5}	1.0358×10^{-5}
$2s^22p^6\ 3d\ ^2D_{3/2}$	$2p^53d\ (^3F)\ 4f\ ^4I_{11/2}$	9.302	9.2469×10^{10}	5.9969×10^{-4}	7.3453×10^{-5}
$2s^22p^6\ 3d\ ^2D_{3/2}$	$2p^53d\ (^1F)\ 4f\ ^2I_{13/2}$	9.292	4.9919×10^{12}	9.6927×10^{-2}	1.1860×10^{-2}
$2s^22p^6\ 3d\ ^2D_{3/2}$	$2p^53d\ (^1P)\ 4d\ ^2D^o_{5/2}$	9.284	6.8304×10^{10}	1.3239×10^{-3}	1.6186×10^{-4}
$2s^22p^6\ 3d\ ^2D_{3/2}$	$2p^53d\ (^3F)\ 4f\ ^4H_{7/2}$	9.280	1.8932×10^{12}	2.4442×10^{-2}	2.9868×10^{-3}
$2s^22p^6\ 3d\ ^2D_{3/2}$	$2p^53d\ (^1P)\ 4d\ ^2P^o_{3/2}$	9.272	7.2929×10^{11}	9.3999×10^{-3}	1.1477×10^{-3}
$2s^22p^6\ 3d\ ^2D_{3/2}$	$2p^53d\ (^1D)\ 4f\ ^2P_{1/2}$	9.264	2.0114×10^{11}	1.2939×10^{-3}	1.5784×10^{-4}
$2s^22p^6\ 3d\ ^2D_{5/2}$	$2p^53d\ (^1D)\ 4d\ ^2S^o_{1/2}$	9.337	7.0642×10^{12}	1.2311×10^{-1}	2.2706×10^{-2}
$2s^22p^6\ 3d\ ^2D_{5/2}$	$2p^53d\ (^3P)\ 4d\ ^2F^o_{7/2}$	9.335	6.4597×10^{12}	5.6257×10^{-2}	1.0373×10^{-2}
$2s^22p^6\ 3d\ ^2D_{5/2}$	$2p^53d\ (^1F)\ 4d\ ^2P^o_{3/2}$	9.333	1.7046×10^{11}	1.4839×10^{-3}	2.7354×10^{-4}
$2s^22p^6\ 3d\ ^2D_{5/2}$	$2p^53d\ (^3D)\ 4d\ ^4S^o_{3/2}$	9.329	1.0654×10^{9}	1.3901×10^{-5}	2.5615×10^{-6}
$2s^22p^6\ 3d\ ^2D_{5/2}$	$2p^53d\ (^1F)\ 4f\ ^2I_{13/2}$	9.297	2.0000×10^{11}	2.5916×10^{-3}	4.7591×10^{-4}
$2s^22p^6\ 3d\ ^2D_{5/2}$	$2p^53d\ (^1P)\ 4d\ ^2D^o_{5/2}$	9.289	8.7382×10^{11}	1.1303×10^{-2}	2.0738×10^{-3}
$2s^22p^6\ 3d\ ^2D_{5/2}$	$2p^53d\ (^3F)\ 4f\ ^4H_{7/2}$	9.285	1.9302×10^{11}	1.6629×10^{-3}	3.0498×10^{-4}
$2s^22p^6\ 3d\ ^2D_{5/2}$	$2p^53d\ (^3F)\ 4f\ ^2D_{3/2}$	9.284	4.4543×10^{10}	7.6750×10^{-4}	1.4075×10^{-4}
$2s^22p^6\ 3d\ ^2D_{5/2}$	$2p^53d\ (^1P)\ 4d\ ^2P^o_{3/2}$	9.277	2.9984×10^{11}	2.5791×10^{-3}	4.7262×10^{-4}

TABLE V. Table for the configuration of F-like lines.

Level	Label	J	Level	Label	j	Level	Label	j
1	$2s^22p^5\ ^2P$	3/2	179	$2s^22p^44d^1\ ^4P$	1/2	282	$2s^22p^45p^{12}P$	3/2
2	$2s^22p^5\ ^2P$	1/2	180	$2s^22p^44d^1\ ^4D$	3/2	283	$2s^22p^45p^{12}D$	3/2
3	$2s^12p^{62}S$	1/2	182	$2s^22p^44d^1\ ^4P$	5/2	284	$2s^12p^54d^{12}D$	5/2
110	$2s^22p^44s^1\ ^2D$	5/2	183	$2s^22p^44d^1\ ^4P$	3/2	285	$2s^22p^45p^{12}P$	1/2
111	$2s^22p^44s^1\ ^2D$	3/2	184	$2s^22p^44d^1\ ^4D$	1/2	286	$2s^12p^54d^{12}F$	7/2
114	$2s^22p^44s^1\ ^2S$	1/2	208	$2s^12p^54p^1\ ^4P$	5/2	287	$2s^12p^54d^{12}P$	3/2
120	$2s^22p^44s^1\ ^2P$	3/2	209	$2s^12p^54p^1\ ^2D$	3/2	288	$2s^12p^54d^{12}F$	5/2
121	$2s^22p^44s^1\ ^2P$	1/2	210	$2s^22p^45s^{12}D$	3/2	289	$2s^12p^54d^{12}P$	1/2
125	$2s^22p^44s^1\ ^4P$	5/2	213	$2s^12p^54s^{12}P$	1/2	293	$2s^12p^54d^{12}D$	3/2
126	$2s^22p^44s^1\ ^4P$	3/2	215	$2s^22p^45p^{12}P$	3/2	297	$2s^12p^54s^{14}P$	3/2
128	$2s^22p^44d^1\ ^2D$	5/2	218	$2s^22p^45p^{12}P$	1/2	305	$2s^12p^54s^{14}P$	1/2
130	$2s^22p^44d^1\ ^2P$	3/2	221	$2s^22p^45p^{12}D$	3/2	316	$2s^22p^45p^{14}S$	3/2
131	$2s^22p^44d^1\ ^2S$	1/2	225	$2s^12p^54d^{12}P$	1/2	317	$2s^22p^45p^{14}D$	5/2
136	$2s^22p^44d^1\ ^2P$	1/2	226	$2s^12p^54d^{12}P$	3/2	318	$2s^12p^54d^{14}P$	3/2
139	$2s^22p^44d^1\ ^2D$	3/2	240	$2s^22p^45s^{12}P$	3/2	319	$2s^22p^45p^{14}P$	3/2
140	$2s^22p^44d^1\ ^2F$	5/2	241	$2s^22p^45s^{12}P$	1/2	320	$2s^22p^45p^{14}P$	1/2
152	$2s^22p^44d^1\ ^2D$	3/2	242	$2s^22p^45d^{12}D$	3/2	328	$2s^22p^45f^{12}D$	5/2
155	$2s^22p^44d^1\ ^2D$	5/2	243	$2s^12p^54d^{12}D$	3/2	345	$2s^22p^45f^{14}D$	1/2
159	$2s^22p^44d^1\ ^2P$	1/2	245	$2s^22p^45p^{12}P$	1/2	346	$2s^22p^45f^{14}F$	3/2
160	$2p^63d^1\ ^2D$	3/2	246	$2s^12p^54p^{12}P$	1/2	351	$2s^22p^45f^{14}D$	3/2
162	$2s^22p^44d^1\ ^2P$	3/2	253	$2s^12p^54p^{14}S$	3/2	370	$2s^22p^45p^{14}D$	1/2
163	$2p^63d^1\ ^2D$	5/2	257	$2s^22p^45f^{12}D$	3/2	371	$2s^22p^45p^{14}D$	3/2
164	$2s^22p^44d^1\ ^2F$	5/2	264	$2s^22p^45f^{12}P$	3/2	407	$2s^12p^55d^{12}D$	3/2
165	$2s^22p^44d^1\ ^2D$	5/2	266	$2s^22p^45p^{12}P$	3/2	408	$2s^12p^55p^{12}P$	3/2
169	$2s^22p^44s^1\ ^4P$	1/2	269	$2s^22p^45f^{12}P$	1/2	410	$2s^12p^55d^{14}P$	1/2
178	$2s^22p^44d^1\ ^4D$	5/2	277	$2s^22p^45p^{12}S$	1/2	424	$2s^12p^55g^{14}F$	3/2
						434	$2s^12p^55s^{12}P$	1/2

observed by comparing spectra from FLYCHK keeping one parameter (either temperature or density) fixed. The synthetic spectrum is plotted for a temperature range of 150–210 eV [Fig. 4(a)] and for a density range of 3×10^{20}–$5 \times 10^{20}/cm^3$ [Fig. 4(b)]. Figure 5 (dotted line) shows the best match regarding the ratio 4C/4D and Na-like satellite/Ne-like resonance at a plasma temperature of 170 eV and a density of $6.5 \times 10^{20}/cm^3$. Fournier *et al.*[30] in their work have shown the effect of varying the escape factor and the fraction of suprathermal electrons on the spectral lines. We included the effect of opacity in our simulation as the level population gets altered with the effects of collisions and photon re-absorption in the plasma. The intensity of a line is a function of the relative abundance of ions and their radiative transition rates and can be written as

$$I_{j,i} = n_j A_{j,i}, \tag{2}$$

which is a function of both the density of ions and the radiative transition rates. In the presence of plasma self-absorption, radiative decay rates are modified $A^{eff} = \varepsilon A_{j,i}$, with ε being the opacity. In our experiment, the plasma is considered to be spherical with a diameter of 100 μm. This influences the distribution of charge states of Cu as shown in Fig. 8(c). Also, the contribution of hot electrons also needs to be taken into account.

So, to accurately determine the ratio of resonance lines which are sensitive to plasma temperature and density, the influence of plasma opacity and the fraction of suprathermal electrons (f) have to be taken into account. This also shifts the ionization balance slightly higher. The effect of opacity in the plasma is already introduced in the simulation. The self-absorption results in a reduction of intensities of the nD lines in comparison to the nC lines. The intensity of our 6C line is more than the 6D resonance line. This indicates a higher opacity in

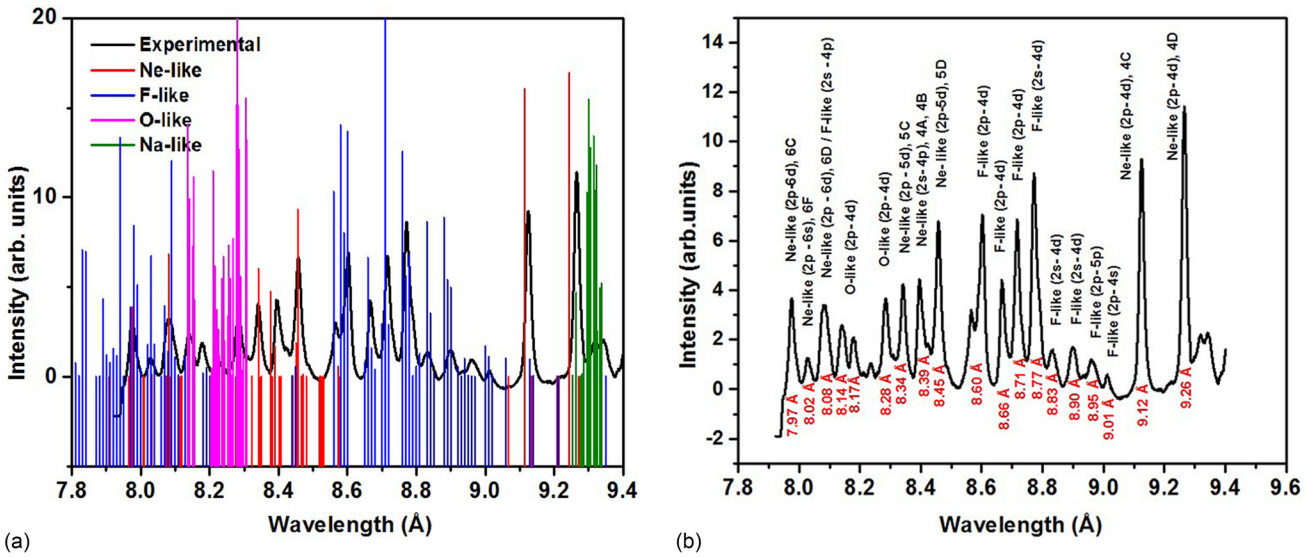

FIG. 2. (a) The experimental spectrum with theoretical predicted line intensity in the spectral range of 7.8 Å–9.4 Å recorded for Ne-, F-, and O-like ions of copper. The relative transition rates are drawn. (b) The labeled experiment spectrum at a laser intensity of 1.3×10^{14} W/cm^2.

our experimentally produced plasma. But, again, it should be borne in mind that this is a time and space integrated spectrum coming out from different regions of the plasma.

The effect of suprathermal electron temperature and fraction on the spectrum on the spectra is considered as follows. Matching between the synthetic and experimental spectra is performed keeping the thermal electron temperature to be around 170 eV, while the suprathermal electron population temperature is varied from 0.5 to 1.5 keV and the ratio of suprathermal to thermal electron temperature is also varied from 0.005 to 0.1. An increase in the suprathermal electron temperature results in an alteration of the satellite to the resonance intensity ratio, and an increase in the fraction of suprathermal electrons raises the abundance of F-like ions and hence corresponding intensity ratios. The increase in the f-value also results in a lowering of the intensity of the Na-like satellite line. The F-like lines are not distinguishable in FLYCHK because it follows the superconfiguration approach, causing these lines to merge together. After several trials using different combinations of T_c, T_h, and f the best match of experimental and stimulated spectra at $T_c = 150$ eV, $T_h = 1000$ eV, $f = 0.008$, and density 4.5×10^{20} cm^{-3} is shown in Fig. 6.

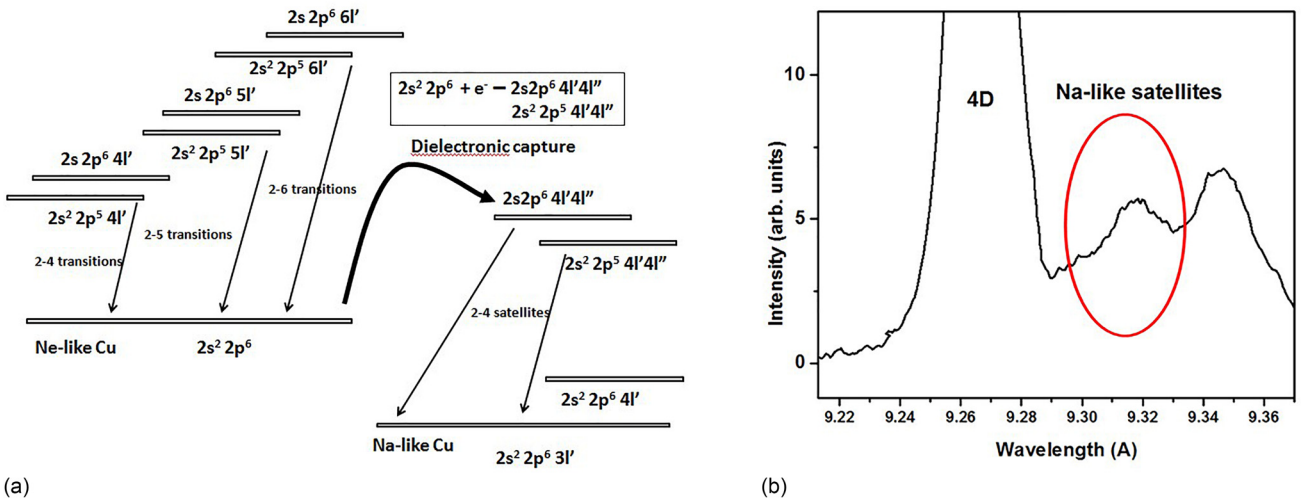

FIG. 3. (a) Energy level diagram of resonance lines from Ne-like Cu and their Na-like satellites. (b) Na-like satellite corresponding to a Ne-like resonance line.

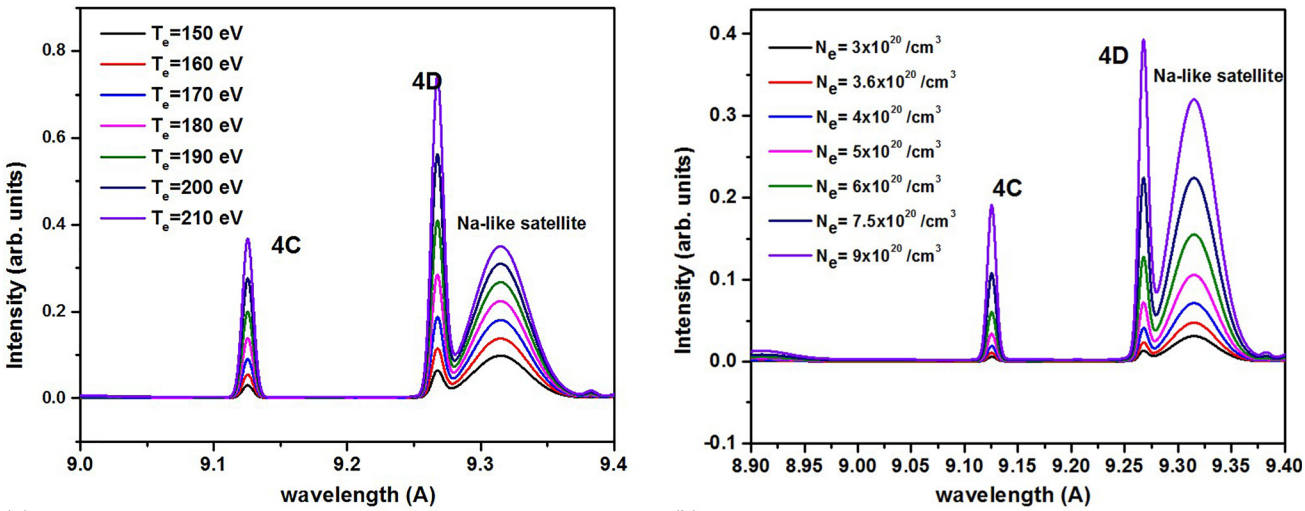

FIG. 4. Dependence of the ratio of 4C to 4D lines and Na-like satellite to 4D line on (a) plasma temperature and (b) electron density as calculated by FLYCHK.

B. Effect of laser intensity on abundance of charge states in plasma

The laser intensity is changed to see the effect on the abundance of ions of different charge states. The spectrum at different laser intensities has been plotted in Fig. 7(a). The intensity of all lines increases with an increase in the intensity of the laser. However, the extent of the change of the intensity of lines from different charge states differs. This is due to the direct dependence of ion charge state populations on the plasma temperature and density. In Figs. 7(b) and 7(c), the zoomed part of the highlighted region is drawn. Four pairs of charge states (labeled as I, II, III, and IV) are compared at varying laser intensities. The first two pairs indicate the increase in O-like Cu ions in comparison to Ne-like and F-like ions and pairs of lines in Secs. III and IV show comparison of F-like with Ne-like ions. When the laser intensity is low (1.3×10^{14} W/cm^2), the intensities of Ne-like ion related emission are enhanced in comparison to F-like and O-like emission indicating the abundance of Cu XX ions in comparison to Cu XXI and Cu XXII ions in the plasma. When the laser intensity increases, the intensity ratio of Ne-like ions to F-like ions (shown in circles III and IV) decreases and the intensity of the F-like line at 8.27 Å has exceeded the intensity of the Ne Like

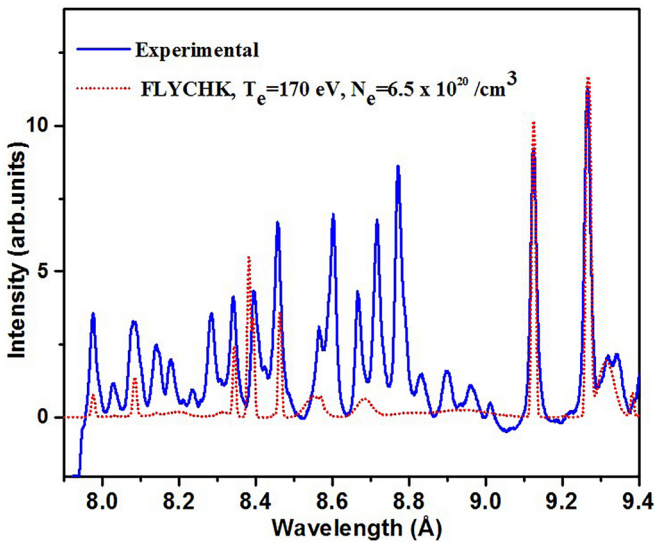

FIG. 5. The experimental spectrum (at 1.3×10^{14} W/cm^2 laser intensity) overlaid with a synthetic spectrum at a plasma temperature of 170 eV and a density of 6.5×10^{20}/cm^3.

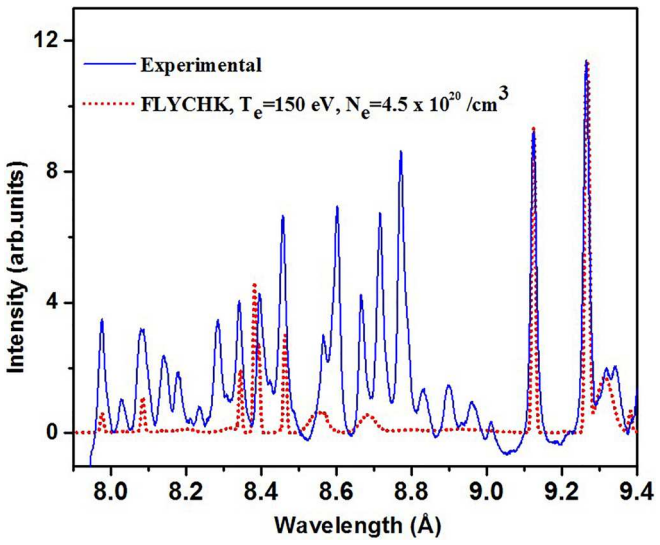

FIG. 6. Best match of the experimental spectrum with the synthetic spectrum at T_c = 150 eV, T_h = 1000 eV, f = 0.008, and density 4.5×10^{20}/cm^3.

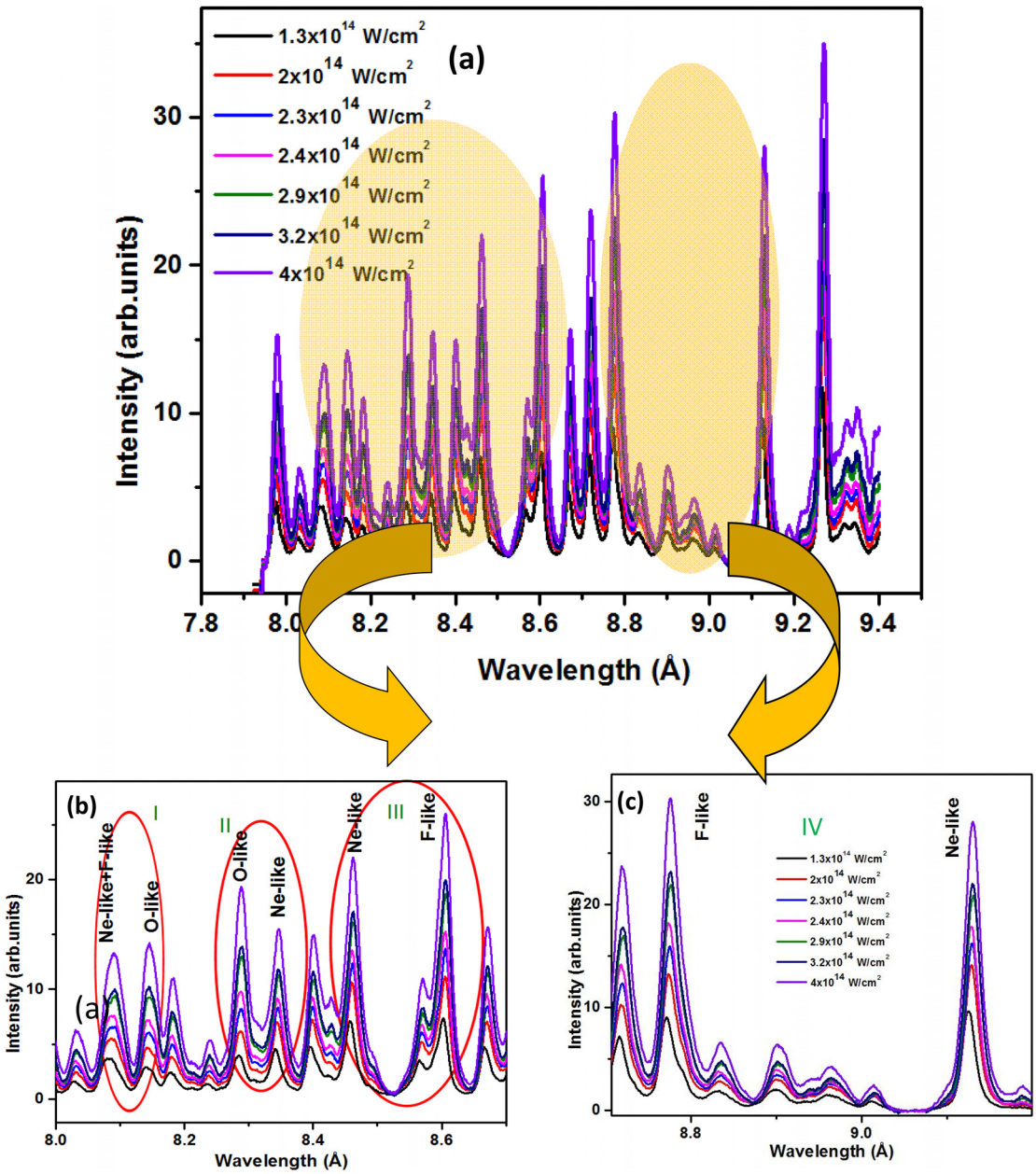

FIG. 7. (a) Experimental spectrum at various laser intensities (b) and (c) zoom of part a to show comparison of population of Ne-like, F-like, and O-like ions at different laser intensities.

line at 9.12 Å at a laser intensity of 2.4×10^{14} W/cm^2, whilst it is lower at a laser intensity of 1.3×10^{14} W/cm^2. These observations indicate that with increased laser intensity, the population of F-like ions relative to Ne-like ions increases. At the same time, it can also be seen that, on further increase in laser intensity, O-like ions become increasingly prominent until O-like emission dominates at 4.0×10^{14} W/cm^2. This indicates that the population of Cu XXII ions is more than the population of F-like and Ne-like ions at this intensity. The difference in intensity from O-like ions as compared to Ne-like ions is large in the circled zone II as compared to zone I. This may be due to the fact that in the circled zone I, the Ne-like line is accompanied by an F-like line and by increasing the laser intensity, the population of both F-like and O-like ions increases which results in the intensity of both lines being increased. At 3.2×10^{14} W/cm^2, O-like emission starts to dominate Ne-like and F-like emission.

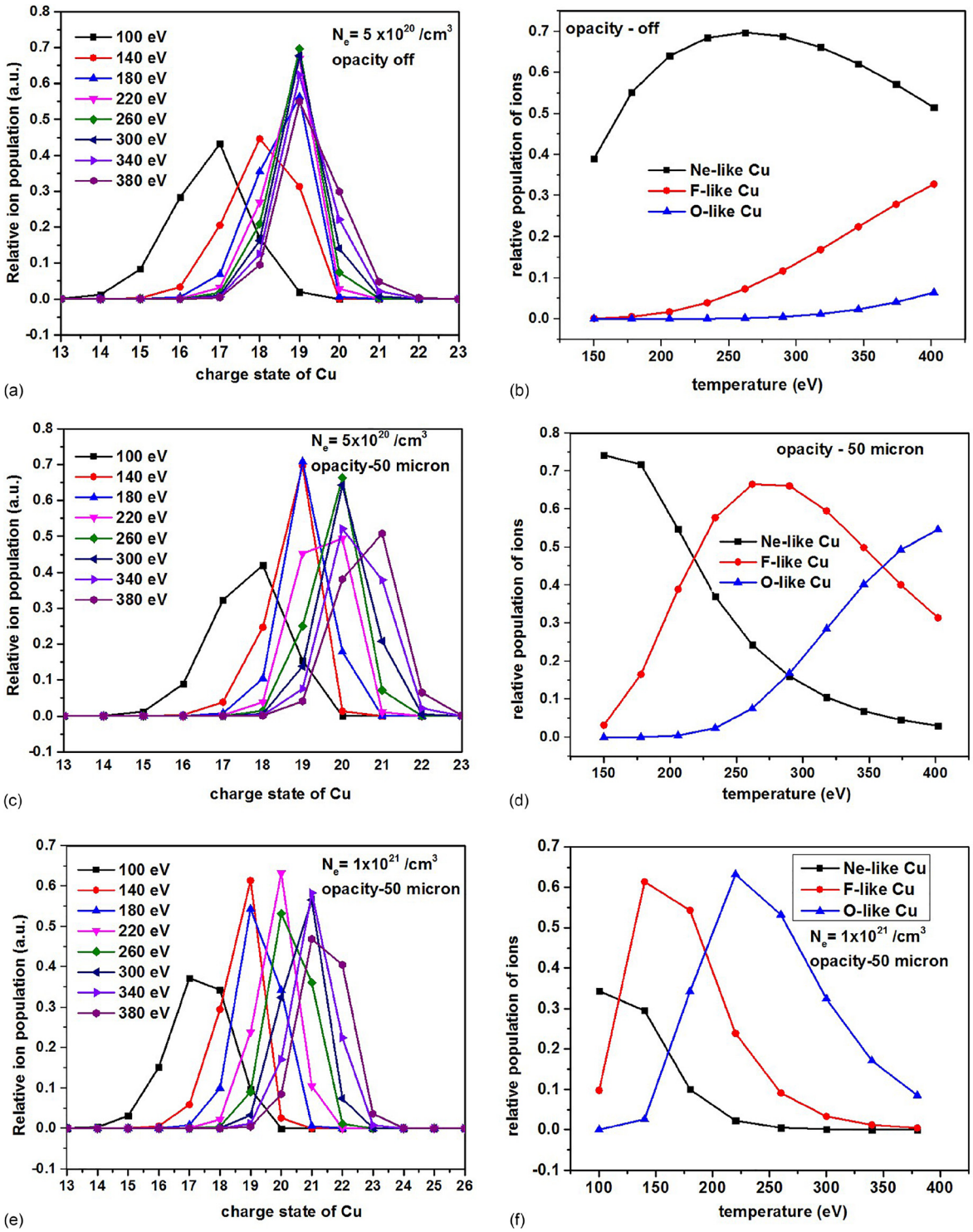

FIG. 8. Distribution of charge states of copper for different temperatures at an electron density of 5×10^{20}/cm^{3}as obtained from FLYCHK simulations (a) without opacity and (b) with opacity. Distribution of Cu XXII (O-like), Cu-XXI (F-like), and Cu-XX (Ne-like) ions at the same electron density as obtained from FLYCHK simulations (c) without opacity and (d) with opacity. Distribution of charge states of Cu at 1×10^{21}/cm^3 as obtained from FLYCHK simulations (e) without opacity and (f) with opacity.

To validate our measurements, we performed FLYCHK simulations to evaluate the charge state distribution and abundance of the charge state of Cu ions at different plasma temperatures and densities with and without the effect of opacity. In the first case, we fixed the plasma density to 5×10^{20} cm^{-3} keeping the opacity off and changing the plasma temperature. The charge state distribution and relative population of the main contributing ions (Ne, F, and O-like Cu ions) at different temperatures are shown in Figs. 8(a) and 8(b). Without opacity, it is observed that the population of Ne-like ions starts dominating at temperatures greater than 150 eV and this continues up to 400 eV. This is against our experimental observation where it has been clearly seen that by increasing the laser intensity (plasma temperature), higher charge states have come to dominate the emission. When the effect of opacity is included, the abundance of F-like ions rises abruptly and their relative population becomes more than the Ne-like Cu above 200 eV as shown in Figs. 8(c) and 8(d). Above 210 eV, the population of O-like lines starts dominating and becomes equal to Ne-like at 280 eV. On further increase in temperature, O-like ions are dominating even over F-like ions at 350 eV.

We have measured plasma temperature and density at a laser intensity of 1.3×10^{14} W/cm^2. For the measurement of temperature and density, we have used only Ne-like lines. FLYCHK is not showing the transitions corresponding to F-like and O-like ions which could otherwise be used for further investigation of plasma temperature and density. The presence of O-like lines for the laser intensity of 1.3×10^{14} W/cm^2, as per Figs. 8(b) and 8(c), indicates that the plasma temperature is 250 eV (where O-like ions start to become apparent).

As already mentioned our integrated spectrum comes from plasma that has large temperature and density gradients. So, X-ray emission is taking place from hotter regions as well as from colder regions. So, at a laser intensity of 1.3×10^{14} W/cm^2, our plasma temperature is in the range of 150–250 eV. When the laser intensity increases, the plasma temperature increases and with it the populations of higher charge states. Dominance of O-like ions over Ne-like and F-like at a laser intensity of 4×10^{14} W/cm^2 indicates that the plasma temperature is of the order of 350 eV from Fig. 8(d) (where O-like starts dominating). So, for the laser intensity 1.3×10^{14} W/cm^2–4×10^{14} W/cm^2, we can say that the plasma temperature ranges from 150 to 350 eV in the region responsible for the bulk of the emission.

To better understand our results, simulations were performed using the 1-D Lagrangian radiation hydrodynamics simulation code HYADES.[44] These simulations used the tabulated SESAME equation of state and a multi-group diffusion approximation for radiation transport based on an average atom LTE ionization model. Electron transport was handled by a flux-limited diffusion approximation. The HYADES results show that there is a region of the plasma that corresponds to the combination of temperature and density conditions that have been estimated above. These simulations further highlight the extremely broad range of plasma density and temperature conditions present, showing temperatures ranging from keV in the low-density corona to below 1 eV in the dense target, with electron densities ranging from below 10^{19} in the corona (Note that since this is a 1-D code the densities will be significantly overestimated in the extremities of the corona.) to above 10^{24} in the shock wave that is propagating into the solid target. Summing over these many different conditions, with appropriate weighting for optical depths, would be required to more accurately reproduce the experimental spectra.

IV. CONCLUSIONS

In summary, we have measured copper spectra from laser irradiated copper targets in the intensity range of 1.3×10^{14} W/cm^2 to 4×10^{14} W/cm^2. The identification of spectral lines and atomic calculations were performed using a Multi-configuration Dirac-Fock (MCDF) method. Lines generated using this simulation are in good agreement with the data available and our experimental results. The average temperature and density of the most strongly radiating portion of the plasma are 150–350 eV and 4.5×10^{20}/cm^3 for laser intensities in the range of 1.3×10^{14}–4×10^{14} W/cm^2. We have performed simulations using the FLYCHK code and performed hydrodynamic simulations which are in good agreement with our experimental results.

ACKNOWLEDGMENTS

The authors from BARC are thankful to Dr. A. K. Mohanty, Director, Physics Group, and Dr. M. N. Deo, Head, LS&FTSS, for their consistent support. The authors are thankful to Shri D. S. Munda, Mr. Ritesh Sable, and Mr. Krishna Bangre for smooth operation of the laser system and for providing support in the data acquisition during the experiment.

REFERENCES

[1]A. Benuzzi-Mounaix, F. Dorchies, V. Recoules, F. Festa, O. Peyrusse, A. Levy, A. Ravasio, T. Hall, M. Koenig, and N. Amadou, Phys. Rev. Lett. **107**(16), 165006 (2011).
[2]J. Zhang, Y. Xu, J. Yang, G. Yang, H. Li, Z. Yuan, Y. Zhao, G. Xiong, L. Bao, and C. Huang, Phys. Plasmas **18**(11), 113301 (2011).
[3]A. Rossall, L. Gartside, S. Chaurasia, S. Tripathi, D. Munda, N. Gupta, L. Dhareshwar, J. Gaffney, S. Rose, and G. Tallents, J. Phys. B: At., Mol. Opt. Phys. **43**(15), 155403 (2010).
[4]L. Antonelli, S. Atzeni, A. Schiavi, S. D. Baton, E. Brambrink, M. Koenig, C. Rousseaux, M. Richetta, D. Batani, P. Forestier-Colleoni, E. Le Bel, Y. Maheut, T. Nguyen-Bui, X. Ribeyre, and J. Trela, Phys. Rev. E **95**(6), 063205 (2017).
[5]J. Lindl, Phys. Plasmas **2**(11), 3933–4024 (1995).
[6]D. Giulietti and L. A. Gizzi, La Riv. Nuovo Cimento (1978-1999) **21**(10), 1–93 (1998).
[7]C. Kaur, S. Chaurasia, A. Poswal, D. Munda, A. Rossall, M. Deo, and S. M. Sharma, J. Quant. Spectrosc. Radiat. Transfer **187**, 20–29 (2017).
[8]L. P. Presnyakov, Sov. Phys. Usp. **19**(5), 387 (1976).
[9]C. Biedermann, R. Radtke, and K. B. Fournier, Phys. Rev. E **66**(6), 066404 (2002).
[10]D. Porquet, J. Dubau, and N. Grosso, Space Sci. Rev. **157**(1-4), 103–134 (2010).
[11]L. Presnyakov and A. Urnov, J. Phys. Colloq. **40**(C7), C7-279–C277-288 (1979).
[12]V. Boiko, A. Y. Faenov, and S. Pikuz, J. Quant. Spectrosc. Radiat. Transfer **19**(1), 11–50 (1978).
[13]U. Safronova, M. Safronova, R. Bruch, and L. Vainshtein, Phys. Scr. **51**(4), 471 (1995).

[14]F. Bely-Dubau, A. Gabriel, and S. Volonté, Mon. Not. R. Astron. Soc. **186**(3), 405–419 (1979).
[15]S. Glenzer, K. Fournier, C. Decker, B. Hammel, R. Lee, L. Lours, B. MacGowan, and A. Osterheld, Phys. Rev. E **62**(2), 2728 (2000).
[16]O. Renner, M. Šmíd, D. Khaghani, and F. B. Rosmej, J. Phys.: Conf. Ser. **688**(1), 012091 (2016).
[17]C. Keane, B. Hammel, D. Kania, J. Kilkenny, R. Lee, A. Osterheld, L. Suter, R. Mancini, C. Hooper, Jr., and N. Delamater, Phys. Fluids B: Plasma Phys. **5**(9), 3328–3336 (1993).
[18]C. Keane, B. Hammel, A. Osterheld, and D. Kania, Phys. Rev. Lett. **72**(19), 3029 (1994).
[19]C. Back, J. Grun, C. Decker, L. Suter, J. Davis, O. Landen, R. Wallace, W. Hsing, J. Laming, and U. Feldman, Phys. Rev. Lett. **87**(27), 275003 (2001).
[20]J. Rice, K. Fournier, M. Graf, L. Terry, M. Finkenthal, F. Bombarda, E. Marmar, and W. Goldstein, Phys. Rev. A **51**(5), 3551 (1995).
[21]G. Brown, P. Beiersdorfer, D. Liedahl, K. Widmann, and S. Kahn, Astrophys. J. **502**(2), 1015 (1998).
[22]N. Brickhouse, A. Dupree, R. Edgar, D. Liedahl, S. Drake, N. White, and K. Singh, Astrophys. J. **530**(1), 387 (2000).
[23]E. Träbert, S. Hansen, P. Beiersdorfer, G. Brown, K. Widmann, and H.-K. Chung, Rev. Sci. Instrum. **79**(10), 10E313 (2008).
[24]K. Fournier, C. Constantin, C. Back, L. Suter, H.-K. Chung, M. Miller, D. Froula, G. Gregori, S. Glenzer, and E. Dewald, J. Quant. Spectrosc. Radiat. Transfer **99**(1–3), 186–198 (2006).
[25]M. Shahzad, G. Tallents, A. Steel, L. Hobbs, D. Hoarty, and J. Dunn, Phys. Plasmas **21**(8), 082702 (2014).
[26]A. Ecuvillon, G. Israelian, N. Santos, M. Mayor, V. Villar, and G. Bihain, Astron. Astrophys. **426**(2), 619–630 (2004).
[27]J. Larour, L. E. Aranchuk, Y. Danisman, A. Eleyan, and M. F. Yilmaz, Phys. Plasmas **23**(3), 033115 (2016).
[28]M. Swartz, S. Kastner, E. Rothe, and W. Neupert, J. Phys. B: At. Mol. Phys. **4**(12), 1747 (1971).
[29]D. Batani, A. Giulietti, L. Palladino, G. J. Tallents, and I. C. E. Turcu, in paper presented at the ECO4 (The Hague'91) (1991).
[30]K. B. Fournier, A. Y. Faenov, T. A. Pikuz, I. Y. Skobelev, V. S. Belyaev, V. I. Vinogradov, A. S. Kyrilov, A. P. Matafonov, I. Bellucci, S. Martellucci, G. Petrocelli, T. Auguste, S. Hulin, P. Monot, and P. D'Oliveira, Phys. Rev. E **67**(1), 016402 (2003).
[31]H. Gordon, M. Hobby, and N. Peacock, J. Phys. B: At. Mol. Phys. **13**(10), 1985 (1980).
[32]K. Fournier, A. Y. Faenov, T. Pikuz, I. Y. Skobelev, F. Flora, S. Bollanti, P. Di Lazzaro, D. Murra, A. Grilli, and A. Reale, J. Phys. B: At., Mol. Opt. Phys. **35**(15), 3347 (2002).
[33]R. Hutcheon, L. Cooke, M. Key, C. Lewis, and G. Bromage, Phys. Scr. **21**(1), 89 (1980).
[34]J. Parkinson, Astron. Astrophys. **24**, 215 (1973).
[35]I. P. Grant, B. J. McKenzie, P. H. Norrington, D. F. Mayers, and N. C. Pyper, Comput. Phys. Commun. **21**(2), 207–231 (1980).
[36]J. Cooper, Rep. Prog. Phys. **29**(1), 35 (1966).
[37]V. Unnikrishnan, K. Alti, V. Kartha, C. Santhosh, G. Gupta, and B. Suri, Pramana **74**(6), 983–993 (2010).
[38]T. Fujimoto and R. W. P. McWhirter, Phys. Rev. A **42**(11), 6588–6601 (1990).
[39]H. K. Chung, M. H. Chen, W. L. Morgan, Y. Ralchenko, and R. W. Lee, High Energy Density Phys. **1**(1), 3–12 (2005).
[40]G. Brown, P. Beiersdorfer, H. Chen, M. Chen, and K. Reed, Astrophys. J. Lett. **557**(1), L75 (2001).
[41]A. Osterheld, J. Nilsen, S. Y. Khakhalin, A. Y. Faenov, and S. Pikuz, Phys. Scr. **54**(3), 240 (1996).
[42]S. Bollanti, P. Di Lazzaro, F. Flora, T. Letardi, L. Palladino, A. Reale, D. Batani, A. Mauri, A. Scafati, and A. Grilli, Phys. Scr. **51**(3), 326 (1995).
[43]R. Bruch, U. Safronova, A. Shlyaptseva, J. Nilsen, and D. Schneider, Phys. Scr. **57**(3), 334 (1998).
[44]p. c. l. c. c. HYADES is a commercial product of Cascade Applied Sciences.